Inorg. Chem. **2005**, *44*, 9213–9224

Syntheses, X-ray Structures, Photochemistry, Redox Properties, and DFT Calculations of Interconvertible *fac*- and *mer*-[Mn(SPS)(CO)$_3$] Isomers Containing a Flexible SPS-Based Pincer Ligand†

Marjolaine Doux, Nicolas Mézailles, Louis Ricard, and Pascal Le Floch*

Laboratoire "Hétéroéléments et Coordination", UMR CNRS 7653, Département de Chimie, Ecole Polytechnique, 92128 Palaiseau Cédex, France

Pedro D. Vaz and Maria José Calhorda*

Departamento de Química e Bioquímica, Faculdade de Ciências da Universidade de Lisboa, 1749-016 Lisboa, Portugal, and Instituto de Tecnologia Química e Biológica (ITQB), Avenida da República, EAN, Apartado 127, 2781-901 Oeiras, Portugal

Taasje Mahabiersing and František Hartl*

Van't Hoff Institute for Molecular Sciences, Universiteit van Amsterdam, Nieuwe Achtergracht 166, 1018 WV Amsterdam, The Netherlands

Received May 13, 2005

The lithium salt of the anionic SPS pincer ligand composed of a central hypervalent λ^4-phosphinine ring bearing two ortho-positioned diphenylphosphine sulfide side arms reacts with [Mn(CO)$_5$Br] to give *fac*-[Mn(SPS)(CO)$_3$]. This isomer can be converted photochemically to *mer*-[Mn(SPS)(CO)$_3$], with a very high quantum yield (0.80 ± 0.05). The thermal backreaction is slow (taking ca. 8 h at room temperature), in contrast to rapid electrode-catalyzed *mer*-to-*fac* isomerization triggered by electrochemical reduction of *mer*-[Mn(SPS)(CO)$_3$]. Both geometric isomers of [Mn(SPS)(CO)$_3$] have been characterized by X-ray crystallography. Both isomers show luminescence from a low-lying ^{3}IL (SPS-based) excited state. The light emission of *fac*-[Mn(SPS)(CO)$_3$] is largely quenched by the efficient photoisomerization occurring probably from a low-lying Mn-CO dissociative excited state. Density functional theory (DFT) and time-dependent DFT calculations describe the highest occupied molecular orbital (HOMO) and lowest unoccupied molecular orbital (LUMO) of *fac*- and *mer*-[Mn(CO)$_3$(SPS)] as ligand-centered orbitals, largely localized on the phosphinine ring of the SPS pincer ligand. In line with the ligand nature of its frontier orbitals, *fac*-[Mn(SPS)(CO)$_3$] is electrochemically reversibly oxidized and reduced to the corresponding radical cation and anion, respectively. The spectroscopic (electron paramagnetic resonance, IR, and UV–vis) characterization of the radical species provides other evidence for the localization of the redox steps on the SPS ligand. The smaller HOMO–LUMO energy difference in the case of *mer*-[Mn(CO)$_3$(SPS)], reflected in the electronic absorption and emission spectra, corresponds with its lower oxidation potential compared to that of the *fac* isomer. The thermodynamic instability of *mer*-[Mn(CO)$_3$(SPS)], confirmed by the DFT calculations, increases upon one-electron reduction and oxidation of the complex.

Introduction

The coordination chemistry of terdentate pincer ligands[1] is a rapidly growing field. Attention is paid to both catalysis[2] and the development of building blocks for novel molecular materials.[3] This class of complexes provides the opportunity to tune subtly electronic properties of the metal center and to control its reactivity by different combinations of the three

* To whom correspondence should be addressed. E-mail: lefloch@poly.polytechnique.fr (P.L.), mjc@fc.ul.pt (M.J.C.), f.hartl@uva.nl (F.H.).

† Dedicated to the memory of the late Professor Dick Stufkens (University of Amsterdam), in recognition of his significant contribution to the field of photochemistry and photophysics of coordination compounds.

(1) van Koten, G. *Pure Appl. Chem.* **1989**, *61*, 1681−1694.

(2) (a) Albrecht, M.; van Koten, G. *Angew. Chem., Int. Ed.* **2001**, *40*, 3750−3781. (b) Albrecht, M.; van Koten, G. *Angew. Chem.* **2001**, *113*, 3866−3878. (c) van der Boom, M. E.; Milstein, D. *Chem. Rev.* **2003**, *103*, 1759−1792. (d) Singleton, J. T. *Tetrahedron Lett.* **2003**, *59*, 1837−1857.

10.1021/ic050774m CCC: $30.25 © 2005 American Chemical Society
Published on Web 10/28/2005

Scheme 1

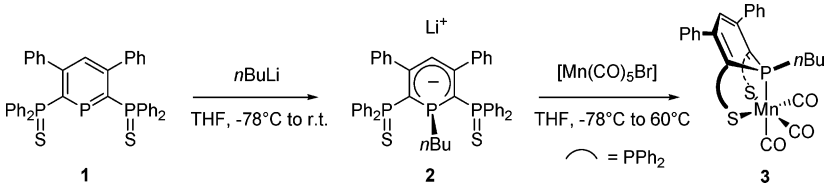

ligand binding sites. The common feature of pincer ligands is their central aromatic ring, usually based on 2,6-disubstituted benzene (XCX type) or pyridine (XNX type), where the X's are the chelating pendant side arms with a variety of donor heteroatom combinations (C, N, O, P, and S).[4]

As a part of our continued research efforts to develop and employ in catalysis sp^2-hybridized P ligands (phosphinines),[5] a novel SPS type of pincer ligand has recently been introduced, based on a central λ^4-phosphinine ring bearing a hypervalent P atom and ancillary phosphine sulfides ($-Ph_2P{=}S$).[6] The precursor compound is the corresponding phosphinine derivative that readily undergoes a nucleophilic attack on the electropositive P atom of the central subunit, for example, with *n*-BuLi (Scheme 1). The peculiar electronic and coordinative properties of the SPS-based anionic tridentate ligands have been systematically investigated. So far, complexes have been prepared and characterized with group 9 [Rh(I), Rh(III), and Ir(I)],[7] 10 [Ni(II), Pd(II), and Pt(II)],[6] and 11 [Cu(I) and Au(I)][8] metals. Very interesting are the Rh(I) complexes that were prepared in two principal coordination geometries: (a) four-coordinate and square planar, where the SPS ligand binds as a classical rigid pincer in an in-plane arrangement (even though the SPS ligand itself is nonplanar), and (b) five-coordinate and trigonal bipyramidal, where the SPS ligand adopts a facial coordination mode, capping one of the triangular faces. The latter arrangement has also been found in a pseudooctahedral rhodium(III) peroxo complex.[7]

The apparent flexibility of the SPS-based tripodate ligands prompted us to attempt the synthesis and thorough characterization of a pseudooctahedral tricarbonyl complex with a formally Mn(I) center, $[Mn(SPS)(CO)_3]$. A number of manganese(I) carbonyls with redox-active ligands have been known to undergo isomerization reactions induced thermally, electrochemically, or photochemically.[9,10] The main goal of this study was to examine the capability of the selected anionic SPS ligand (**2** in Scheme 1) to adopt different spatial arrangements in $[Mn(SPS)(CO)_3]$. A comparative study of the bonding, spectroscopic, photochemical, and redox properties of the envisaged *fac*- and *mer*-$[Mn(SPS)(CO)_3]$ isomers and their interconversion was also at the center of our interest (Scheme 2). Density functional theory (DFT) calculations were employed to support the experimental data.

Scheme 2

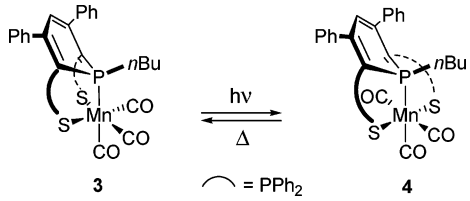

Experimental Section

General Remarks. All reactions and experiments were performed under an inert atmosphere of dry argon or nitrogen, using Schlenk and glovebox techniques and dry deoxygenated solvents. The solutions of highly photoreactive complex **3** were handled under exclusion of daylight.

Dry THF and hexanes were obtained by distillation from sodium benzophenone, dry diethyl ether from $CaCl_2$ and then NaH, and dry CH_2Cl_2 from P_2O_5. $CDCl_3$ was distilled from P_2O_5 and stored on 4-Å Linde molecular sieves. CD_2Cl_2 was used as purchased and stored under argon in a glovebox. The supporting electrolyte, tetrabutylammonium hexafluorophosphate (Bu_4NPF_6; Aldrich), was recrystallized twice from absolute ethanol and dried overnight at 80 °C under vacuum before use. Ferrocene (Fc; BDH) and 2,2-diphenyl-1-picrylhydrazyl (DDPH; Aldrich) were used as received. Phosphinine **1** and anion **2**,[6] $[Mn(CO)_5Br]$[11] and $FcBF_4$,[12] were prepared according to reported procedures. Elemental analyses were performed by Service d'analyze du CNRS, Gif-sur-Yvette, France.

(3) (a) Rodríguez, G.; Albrecht, M.; Schoenmaker, J.; Ford, A.; Lutz, M.; Spek, A. L.; van Koten, G. *J. Am. Chem. Soc.* **2002**, *124*, 5127−5138. (b) Ghedini, M.; Pucci, G.; Crispini, A.; Aiello, I.; Barigelletti, F.; Gessi, A.; Francescangeli, O. *Appl. Organomet. Chem.* **1999**, *13*, 565−581. (c) Aiello, I.; Dattilo, D.; Ghedini, M.; Bruno, A.; Termine, R.; Golemme, A. *Adv. Mater.* **2002**, *14*, 1233−1236. (d) Talarico, M.; Barberio, G.; Pucci, D.; Ghedini, M.; Golemme, A. *Adv. Mater.* **2003**, *15*, 1374−1377. (e) Gagliardo, M.; Dijkstra, H. P.; Coppo, P.; De Cola, L.; Lutz, M.; Spek, A. L.; van Klink, G. P. M.; van Koten, G. *Organometallics* **2004**, *23*, 5833−5840.

(4) Díez-Barra, E.; Guerra, J.; López-Solera, I.; Meriono, S.; Rodríguez-López, J.; Sánchez-Verdú, P.; Tejeda, J. *Organometallics* **2003**, *22*, 541−547 and references cited therein.

(5) (a) Le Floch, P.; Mathey, F. *Coord. Chem. Rev.* **1998**, *179*−*180*, 771−791. (b) Mézailles, N.; Matthey, F.; Le Floch, P. *Prog. Inorg. Chem.* **2001**, *49*, 455−550.

(6) (a) Doux, M.; Mézailles, N.; Melaimi, M.; Ricard, L.; Le Floch, P. *Chem. Commun.* **2002**, 1566−1567. (b) Doux, M.; Bouet, C.; Mézailles, N.; Ricard, L.; Le Floch, P. *Organometallics* **2002**, *21*, 2785−2788. (c) Doux, M.; Mézailles, N.; Ricard, L.; Le Floch, P. *Eur. J. Inorg. Chem.* **2003**, 3878−3894.

(7) (a) Doux, M.; Mézailles, N.; Ricard, L.; Le Floch, P. *Organometallics* **2003**, *22*, 4624−4626. (b) Doux, M.; Ricard, L.; Le Floch, P.; Jean, Y. *Organometallics* **2005**, *24*, 1608−1613. (c) Doux, M.; Le Floch, P.; Jean, Y. *Theor. Chem.* **2005**, *724*, 73−79.

(8) Doux, M.; Ricard, L.; Le Floch, P.; Mézailles, N. *Dalton Trans.* **2004**, 2593−2600.

(9) (a) Carriedo, G. A.; Crespo, M. C.; Diaz, C.; Riera, V. *J. Organomet. Chem.* **1990**, *397*, 309−312. (b) Brown, N. C.; Carriedo, G. A.; Connelly, N. G.; Garcia Alonso, F. J.; Quermby, I. C.; Rieger, A. L.; Rieger, P. H.; Riera, V.; Vivanco, M. *J. Chem. Soc., Dalton Trans.* **1994**, 3745−3752.

(10) (a) Stor, G. J.; Morrison, S. L.; Stufkens, D. J.; Oskam, A. *Organometallics* **1994**, *13*, 2641−2650. (b) Kleverlaan, C. J.; Hartl, F.; Stufkens, D. J. *J. Photochem. Photobiol., A* **1997**, *103*, 231−237. (c) Rossenaar, B. D.; Hartl, F.; Stufkens, D. J.; Amatore, C.; Maisonhaute, E.; Verpeaux, J.-N. *Organometallics* **1997**, *16*, 4675−4685.

(11) Quick, M. H.; Angelici, R. J. *Inorg. Synth.* **1979**, *19*, 160−161 and 163.

(12) Hendrickson, D. N.; Sohn, Y. S.; Gray, H. B. *Inorg. Chem.* **1971**, *10*, 1559−1563.

Synthesis of Complex 3. A solution of 1.6 M *n*-BuLi in hexanes (0.637 mL, 0.59 mmol) was syringed into a solution of **1** (400 mg, 0.59 mmol) in THF (20 mL) at −78 °C. The solution was warmed to room temperature and stirred for 20 min. Complete formation of **2** was checked by ^{31}P NMR (121.5 MHz, THF, 298 K): δ 45.8 (d, $^2J(P_A-P_X) = 156.0$ Hz, P_XPh_2), −66.2 (AX_2, t, $^2J(P_A-P_X) = 156.0$ Hz, P_ABu). After cooling to −78 °C, $[Mn(CO)_5Br]$ (164 mg, 0.59 mmol) was added, and the solution was warmed to room temperature and stirred for 16 h at 65 °C. After removal of the solvent, the resulting solid was dissolved in CH_2Cl_2 (100 mL) and filtered through Celite. After evaporation of the solvent under vacuum, the residue was washed several times with hexanes (2 × 5 mL) and diethyl ether (2 × 5 mL). After drying, product **3** was collected as a yellow solid. Crystals suitable for X-ray analysis deposited after cooling a solution of **3** in hot CH_2Cl_2 back to room temperature. Yield: 422 mg, 82%. ^{31}P NMR (121.5 MHz, THF, 298 K): δ 57.5 (d, $^2J(P_A-P_X) = 119.7$ Hz, P_XPh_2), 82.7 (AX_2, t, $^2J(P_A-P_X) = 119.7$ Hz, P_A). ^{1}H NMR (300 MHz, $CDCl_3$, 298 K): δ 1.00 (m, $\Sigma J = 18.7$ Hz, 3H, CH_3), 1.50 (m, $\Sigma J = 21.7$ Hz, 2H, CH_2), 1.85 (m, $\Sigma J = 25.6$ Hz, 2H, CH_2), 2.31 (m, $\Sigma J = 24.9$ Hz, 2H, CH_2), 5.79 (t, $\Sigma J = 11.2$ Hz, 1H, H_4), 6.80−8.06 (m, 30H, CH of Ph). Complex **3** is not sufficiently soluble to collect its ^{13}C NMR spectrum. IR (THF): 2013s, 1934m, 1909m cm^{-1}. Calcd for $C_{48}H_{40}MnO_3P_3S_2$ (876.10): C, 65.75; H, 4.60. Found: C, 65.41; H, 4.27.

Synthesis of Complex 4. A solution of **3** (20 mg, 0.025 mmol) in THF (0.5 mL) in a sealed NMR tube was immersed in a photoreactor (400 mL) filled with water. The solution was irradiated at room temperature for ca. 6 h with a TQ-150 Heraeus medium-pressure Hg lamp. After drying, complex **4** was obtained as an orange solid in a nearly quantitative yield. Crystals of **4** suitable for X-ray analysis deposited overnight in a CH_2Cl_2 solution that was continuously irradiated with visible light in order to prevent the thermal isomerization to complex **3**. ^{31}P NMR (121.5 MHz, THF, 298 K): δ 47.6 (AX_2, t, $^2J(P_A-P_X) = 127.5$ Hz, P_A), 58.2 (d, $^2J(P_A-P_X) = 127.5$ Hz, P_XPh_2). ^{1}H NMR (300 MHz, CD_2Cl_2, 298 K): δ 1.00 (bs, 3H, CH_3), 1.50 (bs, 2H, CH_2), 1.83 (bs, 2H, CH_2), 2.25 (bs, 2H, CH_2), 5.58 (bs, 1H, H_4), 7.02−8.08 (m, 30H, CH of Ph). Complex **4** is not sufficiently soluble to obtain a ^{13}C NMR spectrum. IR (THF): 2024w, 1930s, 1915m cm^{-1}.

Spectroscopic Measurements. NMR spectra were recorded on a Bruker Advance 300 spectrometer operating at 300.0 MHz for ^{1}H nuclei and 121.5 MHz for ^{31}P nuclei. Solvent signals were used as internal references relative to Me_4Si for ^{1}H NMR chemical shifts (ppm); ^{31}P NMR chemical shifts are given relative to a 85% H_3PO_4 external reference. Coupling constants are given in hertz. Electron paramagnetic resonance (EPR) spectra were recorded with a Varian Century E-104A X-band spectrometer and simulated with the programs PEST Winsim (version 0.96)[13] and Bruker WINEPR SimFonia (version 1.25). IR spectra were obtained with a Bio-Rad FTS-7 FTIR spectrometer (16 scans, resolution of 2 cm^{-1}). The following abbreviations are used: (NMR) s, singlet; d, doublet; t, triplet; m, multiplet; b, broad; (IR) s, strong; m, medium; w, weak. Electronic absorption spectra were recorded using a Hewlett-Packard 8453A diode-array spectrophotometer.

Emission Spectroscopy. Continuous-wave emission spectra were obtained on a Spex Fluorolog 1681 spectrofluorimeter equipped with a Xe arc light source, a Hamamatsu R928 photomultiplier tube detector, and double excitation and emission monochromators. Emission spectra were corrected for source intensity and detector response by standard correction curves. Luminescence quantum yields (Φ_{em}) were measured in optically diluted solutions ($A \sim 0.1$), using $[Ru(bpy)_3]Cl_2$ ($\Phi_{em} = 0.062$ in deoxygenated acetonitrile[14]) according to the equation[15]

$$\Phi^s_{em} = \Phi^r_{em}(I_s/I_r)(A_r/A_s)(\eta_s/\eta_r)^2 \quad (1)$$

where indexes s and r denote the sample and reference, respectively. I stands for the integrated emission intensity, A is the absorbance at the excitation wavelength, and η is the refractive index of the solvent. Deoxygenated solutions were prepared by freeze−pump−thaw techniques on a high-vacuum line.

Photochemistry. The photochemical conversion of complex **3** to its *mer* isomer, **4**, for spectroscopic and electrochemical measurements was achieved by irradiation of 10^{-3}−10^{-2} M samples for about 1 min with a high-pressure 200-W Hg lamp (Oriel, model 6137), using a 460-nm interference filter. The quantum yield of the photoisomerization in THF at $\lambda_{exc} = 460$ nm and $T = 293$ K was determined using a stable monochromatized output of the medium-pressure Xe lamp of the Spex Fluorolog 1681 spectrofluorimeter. The incident photon flux at the irradiating wavelength, I_0 (2.00×10^{-9} einstein s^{-1}), was measured using the Aberchrome 540P actinometer[16] supplied by Aberchromics Ltd., Wales, U.K. The quantum yield was calculated according to the equation[17]

$$\ln\frac{A - A_\infty}{A_0 - A_\infty} = \frac{\Phi I_0 \epsilon l}{V}\int_0^t \frac{1 - 10^{-A}}{A}\,dt \quad (2)$$

where A, A_0, and A_∞ are the values of the absorbance at λ_{exc} of the sample solution at time t, before the irradiation, and after the completion of photoisomerization and ϵ is the molar absorption coefficient of the starting compound at λ_{exc} (8450 M^{-1} cm^{-1}). The calculated quantum yield Φ is an average value for several irradiating intervals $\Delta t = t_{i+1} - t_i$, leading to changes in A not exceeding 5% of the total absorbance change. The integral in eq 2 was then approximated with $[(t_{i+1} - t_i)/2][(1 - 10^{-A_i})/A_i + (1 - 10^{-A_{i+1}})/A_{i+1}]$. The determination of Φ was repeated three times.

Cyclic Voltammetry and Spectroelectrochemistry. Conventional cyclic voltammograms were recorded with a PAR EG&G model 283 potentiostat, using an airtight, light-protected, single-compartment cell placed in a Faraday cage. The working electrode was a Pt disk (0.42-mm^2 apparent surface area), polished with a 0.25-μm diamond paste between the scans. Coiled Pt and Ag wires served as auxiliary and pseudoreference electrodes, respectively. The sample concentration was typically 10^{-3} mol dm^{-3}. Fc was used as the internal standard[18] for the determination of electrode potentials and comparison of peak-to-peak potential differences. Conversion of the Fc/Fc$^+$ potential scale to other reference systems can be found elsewhere.[19]

IR spectroelectrochemical experiments at low temperatures were performed with a cryostated optically transparent thin-layer electrochemical (OTTLE) cell equipped with CaF_2 windows and a Pt minigrid working electrode (32 wires per centimeter).[20] The IR and

(13) Duling, D. *Public EPR Software Tools*; National Institute of Environmental Health Sciences. http://epr.niehs.nih.gov/pest.html.

(14) Calvert, J. M.; Caspar, J. V.; Binstead, R. A.; Westmoreland, T. D.; Meyer, T. J. *J. Am. Chem. Soc.* **1982**, *104*, 6620−6627.
(15) Demas, J. N.; Crosby, G. A. *J. Phys. Chem.* **1971**, *75*, 991−1024.
(16) Heller, H. G. *J. Chem. Soc., Dalton Trans.* **1981**, 341−343.
(17) Manuta, D. M.; Lees, A. J. *Inorg. Chem.* **1986**, *25*, 1354−1359.
(18) Gritzner, G.; Kùta, J. *Pure Appl. Chem.* **1984**, *56*, 461−466.
(19) Pavlishchuk, V. V.; Addison, A. W. *Inorg. Chim. Acta* **2000**, *298*, 97−102.
(20) (a) Hartl, F.; Luyten, H.; Nieuwenhuis, H. A.; Schoemaker, G. C.; *Appl. Spectrosc.* **1994**, *48*, 1522−1528. (b) Mahabiersing, T.; Luyten, H.; Nieuwendam, R. C.; Hartl, F. *Collect. Czech. Chem. Commun.* **2003**, *68*, 1687−1709.

UV−vis spectroelectrochemistries at room temperature were conducted with another homemade demountable OTTLE cell.[21] The solutions were typically 3×10^{-1} M in the supporting electrolyte and 10^{-3} M (UV−vis) or 5×10^{-3} M (IR) in the analyte. EPR spectroelectrochemical experiments at variable temperatures were carried out with an airtight three-electrode version of the Allendoerfer-type cell equipped with Au-helix working, Pt-helix auxiliary, and Ag-wire pseudoreference electrodes.[22] The solution contained 10^{-3} M complex **3** and 3×10^{-1} M supporting electrolyte. The *g* values were determined against DPPH used as an external standard ($g = 2.0037$).[23] The working-electrode potential of the spectroelectrochemical cells was controlled with a PA4 potentiostat (EKOM, Polná, Czech Republic). A thin-layer cyclic voltammogram was recorded in the course of each spectroelectrochemical experiment to localize the redox events.

Computational Details. DFT calculations[24] were performed with the *Gaussian 03* (G03) and *ADF2004* sets of programs. Under G03,[25] all calculations were carried out within the framework of hybrid DFT, including a mixture of Hartree−Fock exchange with DFT exchange correlation given by the B3PW91 functional.[26] The Hay−Wadt effective core potential (quasi-relativistic for the metal centers) was used for the Mn atom with a (441/2111/41) valence basis set[27] augmented with an f-type polarization function (exponent = 2.195).[28] The 6-311+G* basis set was used for S and P atoms and the 6-31+G* basis set for C atoms bound to the Mn center. The 6-31G* basis set was used for all other atoms (C and H in the SPS ligand and O in the CO ligands). The geometries of model complexes **3m** and **4m** were optimized without any geometry constraints. Harmonic vibrational eigenvalues were calculated at the same level of theory to characterize the stationary points and to determine the zero-point energies. All optimized structures reported have only positive eigenvalues of the Hessian matrix and are minima on the potential energy surface. The frontier orbitals were represented with the MOLEKEL program.[29] The 10 lowest-energy excitations were obtained from time-dependent (TD) calculations, carried out at the same level of theory, using the TD keyword of *Gaussian 03*.[30]

As we could not obtain reliable coefficients for the wave functions derived from the calculations described above, they were repeated upon several different conditions. The B3LYP[31] functional and smaller basis sets (6-31G*[32,33] for C, H, and O; 6-31+G*[32−34] for P and S; lanl2dz[27] for Mn) led to trustful results, which were used in all TD calculations. The geometries were well reproduced in all cases, and the outcome of the TD calculations was qualitatively very similar. The orbital coefficients were obtained from a single-point calculation where diffuse functions were removed from the basis set of P and S.

In the *ADF2004*[35] calculations,[36] Vosko, Wilk, and Nusair's local exchange correlation potential[37] and the PW91 functional[38] with a generalized gradient approximation (GGA) exchange correlation functional[36,39] were used. The core orbitals were frozen for Mn ([1−3]s, [2−3]p), S and P ([1−2]s, 2p), and C and O (1s). Triple-ζ Slater-type orbitals were used to describe the valence shells of H (1s), C and O (2s and 2p), S and P (3s, 3p), and Mn (3d, 4s). A set of two polarization functions was added: H (single ζ, 2p, 3d), C and O (single ζ, 3d, 4f), S and P (single ζ, 3d, 4f), and Mn (single ζ, 4p, 4f). Full geometry optimizations were performed without any symmetry constraints. TD-DFT calculations in the ADF implementation were used to determine the excitation energies. In all cases, the lowest 10 singlet−singlet excitation energies were calculated using the optimized geometries.[40]

X-ray Crystallographic Study. Table 1 contains the structure refinement for **3** and **4.** Complex **3** crystallized with half a CH_2Cl_2 molecule located near the symmetry center. Anisotropic refinement led to nonpositively defined *U*'s for its C atom. Therefore, the solvate was accounted for by using the Platon SQUEEZE function. Crystals of **4** proved to be twinned by 180° rotation about the (−1,

(21) Krejčík, M.; Daněk, M.; Hartl, F. *J. Electroanal. Chem. Interfacial Electrochem.* **1991**, *317*, 179−187.
(22) Hartl, F.; Groenestein, R. P.; Mahabiersing, T. *Collect. Czech. Chem. Commun.* **2001**, *66*, 52−66.
(23) Krzystek, J.; Sienkiewicz, A.; Pardi, L.; Brunel, L. C. *J. Magn. Reson.* **1997**, *125*, 207−211.
(24) Parr, R. G.; Yang, W. *Density-functional theory of atoms and molecules*; Oxford University Press: Oxford, U.K., 1989.
(25) Frisch, M. J.; Trucks, G. W.; Schlegel, H. B.; Scuseria, G. E.; Robb, M. A.; Cheeseman, J. R.; Montgomery, J. A., Jr.; Vreven, T.; Kudin, K. N.; Burant, J. C.; Millam, J. M.; Iyengar, S. S.; Tomasi, J.; Barone, V.; Mennucci, B.; Cossi, M.; Scalmani, G.; Rega, N.; Petersson, G. A.; Nakatsuji, H.; Hada, M.; Ehara, M.; Toyota, K.; Fukuda, R.; Hasegawa, J.; Ishida, M.; Nakajima, T.; Honda, Y.; Kitao, O.; Nakai, H.; Klene, M.; Li, X.; Knox, J. E.; Hratchian, H. P.; Cross, J. B.; Bakken, V.; Adamo, C.; Jaramillo, J.; Gomperts, R.; Stratmann, R. E.; Yazyev, O.; Austin, A. J.; Cammi, R.; Pomelli, C.; Ochterski, J. W.; Ayala, P. Y.; Morokuma, K.; Voth, G. A.; Salvador, P.; Dannenberg, J. J.; Zakrzewski, V. G.; Dapprich, S.; Daniels, A. D.; Strain, M. C.; Farkas, O.; Malick, D. K.; Rabuck, A. D.; Raghavachari, K.; Foresman, J. B.; Ortiz, J. V.; Cui, Q.; Baboul, A. G.; Clifford, S.; Cioslowski, J.; Stefanov, B. B.; Liu, G.; Liashenko, A.; Piskorz, P.; Komaromi, I.; Martin, R. L.; Fox, D. J.; Keith, T.; Al-Laham, M. A.; Peng, C. Y.; Nanayakkara, A.; Challacombe, M.; Gill, P. M. W.; Johnson, B.; Chen, W.; Wong, M. W.; Gonzalez, C.; Pople, J. A. *Gaussian 03*, revision B.04; Gaussian, Inc.: Wallingford, CT, 2004.
(26) Becke, A. D. *J. Chem. Phys.* **1993**, *98*, 5648−5652.
(27) (a) Hay, P. J.; Wadt, W. R. *J. Chem. Phys.* **1985**, *82*, 270−283. (b) Hay, P. J.; Wadt, W. R. *J. Chem. Phys.* **1985**, *82*, 299−310.
(28) Ehlers, A. W.; Böhme, M.; Dapprich, S.; Gobbi, A.; Höllwarth, A.; Jonas, V.; Köhler, K. F.; Stegmann, R.; Veldkamp, A.; Frenking, G. *Chem. Phys. Lett.* **1993**, *208*, 111−114.
(29) (a) Flükiger, P. Development of Molecular Graphics Package MOLEKEL. Ph.D. Thesis, University of Geneva, Geneva, Switzerland, 1992. (b) Portmann, S.; Lüthi, H. P. *Chimia* **2000**, *54*, 766−770.
(30) (a) Stratmann, R. E.; Scuseria, G. E.; Frisch, M. J. *J. Chem. Phys.* **1998**, *109*, 8218−8224. (b) Bauernschmitt, R.; Ahlrichs, R. *Chem. Phys. Lett.* **1996**, *256*, 454−464. (c) Casida, M. E.; Jamorski, C.; Casida, K. C.; Salahub, D. R. *J. Chem. Phys.* **1998**, *108*, 4439−4449.
(31) (a) Lee, C.; Yang, W.; Parr, R. G. *Phys. Rev. B* **1988**, *37*, 785−789. (b) Becke, A. D. *J. Chem. Phys.* **1993**, *98*, 5648−5652.
(32) (a) Ditchfield, R.; Hehre, W. J.; Pople, J. A. *J. Chem. Phys.* **1971**, *54*, 724−728. (b) Hehre, W. J.; Ditchfield, R.; Pople, J. A. *J. Chem. Phys.* **1972**, *56*, 2257−2261. (c) Hariharan, P. C.; Pople, J. A. *Theor. Chim. Acta* **1973**, *28*, 213−222. (d) Hariharan, P. C.; Pople, J. A. *Mol. Phys.* **1974**, *27*, 209−214. (e) Gordon, M. S. *Chem. Phys. Lett.* **1980**, *76*, 163−168.
(33) Frisch, M. J.; Pople, J. A.; Binkley, J. S. *J. Chem. Phys.* **1980**, *80*, 3265−3269.
(34) Clark, T.; Chandrasekhar, J.; Spitznagel, G. W.; Schleyer, P. v. R. *J. Comput. Chem.* **1983**, *4*, 294−301.
(35) Baerends, E. J.; Autschbach, J. A.; Berces, A.; Bo, C.; Boerrigter, P. M.; Cavallo, L.; Chong, D. P.; Deng, L.; Dickson, R. M.; Ellis, D. E.; Fan, L.; Fischer, T. H.; Fonseca Guerra, C.; van Gisbergen, S. J. A.; Groeneveld, J. A.; Gritsenko, O. V.; Grüning, M.; Harris, F. E.; van den Hoek, P.; Jacobsen, H.; van Kessel, G.; Kootstra, F.; van Lenthe, E.; McCormack, D. A.; Osinga, V. P.; Patchkovskii, S.; Philipsen, P. H. T.; Post, D.; Pye, C. C.; Ravenek, W.; Ros, P.; Schipper, P. R. T.; Schreckenbach, G.; Snijders, J. G.; Sola, M.; Swart, M.; Swerhone, D.; te Velde, G.; Vernooijs, P.; Versluis, L.; Visser, O.; van Wezenbeek, E.; Wiesenekker, G.; Wolff, S. K.; Woo, T. K.; Ziegler, T. *ADF2004*; SCM NV: Amsterdam, The Netherlands, 2004.
(36) Fan, L.; Ziegler, T. *J. Chem. Phys.* **1991**, *95*, 7401−7408.
(37) Vosko, S. H.; Wilk, L.; Nusair, M. *Can. J. Phys.* **1980**, *58*, 1200−1211.
(38) Perdew, J. P.; Chevary, J. A.; Vosko, S. H.; Jackson, K. A.; Pederson, M. R.; Singh, D. J.; Fiolhais, C. *Phys. Rev. B* **1992**, *46*, 6671−1687.
(39) Versluis, L.; Ziegler, T. *J. Chem. Phys.* **1988**, *88*, 322−328.
(40) (a) van Gisbergen, S. J. A.; Groeneveld, J. A.; Rosa, A.; Snijders, J. G.; Baerends, E. J. *J. Phys. Chem. A* **1999**, *103*, 6835−6844. (b) Rosa, A.; Baerends, E. J.; van Gisbergen, S. J. A.; van Lenthe, E.; Groeneveld, J. A.; Snijders, J. G. *J. Am. Chem. Soc.* **1999**, *121*, 10356−10365. (c) van Gisbergen, S. J. A.; Rosa, A.; Ricciardi, G.; Baerends, E. J. *J. Chem. Phys.* **1999**, *111*, 2499−2506.

Table 1. Crystal Data and Structural Refinement Details for Complexes **3** and **4**

complex	**3**	**4**
formula	$C_{48}H_{40}O_3P_3MnS_2 \cdot 0.5CH_2Cl_2$	$C_{48}H_{40}MnO_3P_3S_2$
M_r	919.23	876.77
T (K)	150.0(10)	150.0(1)
cryst syst	orthorhombic	monoclinic
space group	*Pbca*	$P2_1$
a (Å)	14.8150(10)	10.3740(10)
b (Å)	22.8510(10)	9.3240(10)
c (Å)	25.5540(10)	22.0760(10)
β (deg)	90.00	91.7340(10)
V (Å^3)	8651.0(8)	2134.4(3)
Z	8	2
ρ (g cm^{-3})	1.412	1.364
μ (cm^{-1})	0. 617	0.561
cryst size (mm)	0.26 × 0.22 × 0.20	0.22 × 0.15 × 0.05
F(000)	3800	908
index ranges	20, 20; −31, 31; −35, 35	−12, 13; −12, 12; −28, 28
scan type	φ and ω scans	φ and ω scans
$2\Theta_{max}$ (deg)/criterion	30.03	27.48
param refined; data/param	515/17	537/32
reflns collcd	23625	20760
independent reflns	12574	20760
reflns used	8984	17631
wR2	0.1394	0.1499
R1	0.0468	0.578
GOF	1.017	1.076
largest diff peak/hole (e Å^{-3})	0.912 (0.074)/ −0.584 (0.074)	0.569 (0.111)/ −0.631 (0.111)

0, 1) lattice direction. Integration of the frames was hence performed accordingly in evalccd.[41] The structure was solved using a non-overlapping subset produced by *SADABS* and subsequently refined as a twin in SHELXL; BASF = 0.498.[42] Data were collected at 150.0(1) K on a Nonius Kappa CCD diffractometer using a Mo Kα (λ = 0.71070 Å) X-ray source and a graphite monochromator. All data were measured using φ and ω scans. Experimental details are described in Table 1. The crystal structures were solved using *SIR97*[43] and *SHELXL-97*.[44] ORTEP drawings were made using *ORTEP-3* for Windows.[45] CCDC 265469 (complex **3**) and 265470 (complex **4**) contain the supplementary crystallographic data for this paper. These data can be obtained free of charge at www.ccdc.cam.ac.uk/conts/retrieving.html [or from the Cambridge Crystallographic Data Centre, 12 Union Road, Cambridge CB2 1EZ, U.K.; fax (international) +44-1223/336-033; e-mail deposit@ccdc.cam.ac.uk].

Results and Discussion

Syntheses and Single-Crystal X-ray Structures. The synthetic route started with λ^3-phosphinine **1** (Scheme 1), which already proved to be a convenient precursor of anion **2** (in the complex formulas abbreviated as SPS).[6] Indeed, the reaction of **1** with *n*-BuLi in THF at low temperature afforded **2** in quantitative yield, as revealed by ^{31}P NMR spectroscopy. Anion **2** then reacted directly in situ with 1 equiv of [Mn(CO)$_5$Br]. After the solution warmed up to room temperature, the reaction was completed by heating at 60 °C overnight. Complex **3** was isolated as an air-stable yellow powder and characterized by ^{31}P and ^{1}H NMR, elemental analysis, and IR spectroscopy. In ^{31}P NMR spectra, complex **3** displays an AX$_2$ spin system pattern. A low-intensity triplet centered at 82.7 ppm ($^2J_{PP}$ = 119.7 Hz) corresponds to the central P atom and a sharper, more intense doublet at 57.5 ppm to the P atom of the P═S moieties. These data suggest that complex **3** adopts a symmetrical structure. Unfortunately, its limited solubility precluded the collection of ^{13}C NMR spectra. For the magnetically equivalent Ph$_2$PS groups of complex **3**, two geometries (*fac* and *mer*) can be proposed. The overall *fac* geometry of the complex was deduced from the characteristic IR ν(CO) pattern that consists of a strong band at 2013 cm^{-1} and two medium-intensity bands at 1934 and 1909 cm^{-1} (in THF).

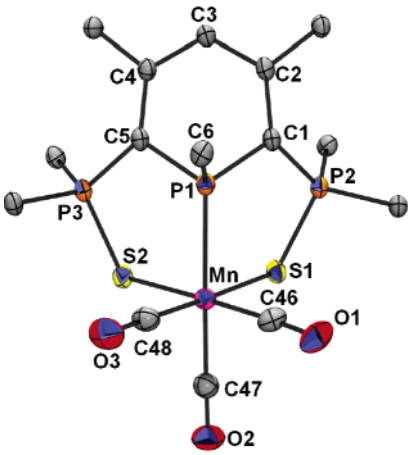

Figure 1. ORTEP view of complex **3**. Ellipsoids are scaled to enclose 50% of the electron density. Phenyl rings and the butyl chain have been omitted for clarity. The numbering is arbitrary and different from that used in NMR data. Selected bond lengths (Å): P1−C1, 1.785(2); C1−C2, 1.413(3); C2−C3, 1.400(3); C3−C4, 1.414(2); C4−C5, 1.403(3); C5−P1, 1.800(2); P1−C6, 1.838(2); C1−P2, 1.760(2); C5−P3, 1.757(2); P2−S1, 2.0212(7); P3−S2, 2.0145(7); C48−O3, 1.155(3); C47−O2, 1.144(3); C46−O1, 1.159(3); P1−Mn, 2.2937(6); S1−Mn, 2.4002(6); S2−Mn, 2.4080(6); C48−Mn, 1.783(2); C47−Mn, 1.829(2); C46−Mn, 1.792(2). Selected angles (deg): C1−P1−C5, 100.72(8); Mn−C46−O1, 177.1(2); Mn−C47−O2, 178.2(2); Mn−C48−O3, 178.3(2); S2−Mn−C46, 177.91(7); S2−Mn−C48, 90.23(8); S2−Mn−S1, 88.01(2); P1−Mn−C47, 172.95(7); (mean plane S2−Mn−C48)−P1, 88.4; (mean plane C1−C2−C4−C5)−P1, 9.0; (mean plane C1−C2−C4−C5)−C3, 23.3; Σ angles at P1, 307.4.

Single crystals of complex **3** suitable for X-ray analysis were grown by crystallization in CH_2Cl_2 at room temperature. A view of one molecule of **3** is presented in Figure 1, with the most significant bond lengths and angles being listed in the legend. Crystal data and structural refinement details are presented in Table 1. Only the *ipso* carbons of the phenyl rings and the P−CH$_2$ part of the butyl group of the SPS ligand have been depicted for clarity. As can be seen, the coordination sphere of the Mn center is close to octahedral. The SPS ligand defines one triangular face of the octahedron, thus confirming the *fac* geometry deduced from the IR spectrum. The ligand is not planar, and the plane defined by C1−P−C5 atoms deviates by 23.3° from the plane defined by C1−C2−C4 and C5. This deviation and the high pyramidality of the P atom (Σ angles at P1 = 307.3°) are commonly encountered in crystal structures of SPS com-

(41) Duisenberg, A. J. M.; Kroon-Batenburg, L. M. J.; Schreurs, A. M. M. *J. Appl. Crystallogr.* **2003**, *36*, 220−229.
(42) Sheldrick, G. M. *SADABS: A Program for Absorption Correction of Crystallographic Data*; Universität Göttingen: Göttingen, Germany, 1996.
(43) Altomare, A.; Burla, M. C.; Camalli, M.; Cascarano, G.; Giacovazzo, C.; Guagliardi, A.; Moliterni, A. G. G.; Polidori, G.; Spagna, R. *SIR97, an integrated package of computer programs for the solution and refinement of crystal structures using single-crystal data*; Institute of Crystallography: Bari, Italy, 1988.
(44) Sheldrick, G. M. *SHELXL-97*; Universität Göttingen: Göttingen, Germany, 1997.
(45) Farrugia, L. J. *ORTEP-3*; Department of Chemistry, University of Glasgow: Glasgow, Scotland, 2003.

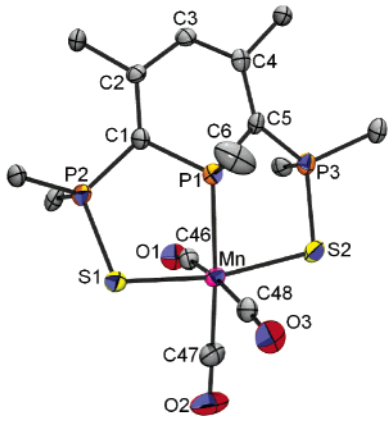

Figure 2. ORTEP view of complex **4**. Ellipsoids are scaled to enclose 50% of the electron density. Phenyl rings and the *n*-Bu chain have been omitted for clarity. The numbering is arbitrary and different from that used in NMR data. Selected bond lengths (Å): P1−C1, 1.783(4); C1−C2, 1.398(5); C2−C3, 1.413(5); C3−C4, 1.399(5); C4−C5, 1.412(5); C5−P1, 1.784(4); P1−C6, 1.832(4); C1−P2, 1.765(4); C5−P3, 1.766(4); P2−S1, 2.034(2); P3−S2, 2.030(2); C48−O3, 1.151(5); C47−O2, 1.158(5); C46−O1, 1.147(4); P1−Mn, 2.2937(6); S1−Mn, 2.401(1); S2−Mn, 2.409(1); C48−Mn, 1.831(4); C47−Mn, 1.797(4); C46−Mn, 1.858(4). Selected angles (deg): C1−P1−C5, 100.8(2); Mn−C46−O1, 170.3(3); Mn−C47−O2, 178.9(5); Mn−C48−O3, 173.6(3); C46−Mn−C48, 170.5(2); S1−Mn−C46, 94.2(1); P1−Mn−C47, 176.4(2); S2−Mn−S1, 165.14(3); (mean plane S1−Mn−C46)−P1, 83.3; (mean plane C1−C2−C4−C5)−P1, 4.8; (mean plane C1−C2−C4−C5)−C3, 19.8; Σ angles at P1, 311.4.

plexes with different transition metals.[6−8] The SPS internal bonding parameters that reflect the electronic nature of the ligand are discussed below for both the *fac* and *mer* isomer geometries.

As described in detail hereafter, irradiation of **3** in THF at room temperature, for example, with sunlight or a Hg lamp, results in efficient *fac*-to-*mer* photoisomerization to complex **4** manifested by a progressive change of the color of the solution from yellow (λ_{max} = 471 nm) to orange-red (λ_{max} = 498 nm). The IR spectrum of **4** shows in the carbonyl stretching region a characteristic band pattern of three carbonyl ligands arranged in *mer* geometry: 2024w, 1930s, and 1915m cm^{-1} (THF). Similarly to precursor **3**, *mer* isomer **4** exhibits a well-resolved ^{31}P NMR spectrum with an AX_2 pattern. Interestingly, the doublet signal of the Ph_2PS moieties in **4** (58.2 ppm, $^2J_{PP}$ = 127.5 Hz) hardly moved upon isomerization ($\Delta\delta$ = +0.7 ppm), whereas the triplet signal due to the central P atom shifted significantly toward the high field ($\Delta\delta$ = −35.2 ppm). Complex **4** in solution is thermally unstable in the dark, and complete recovery of *fac* isomer **3** was observed within 8 h at room temperature (Scheme 2).

The *mer* geometry of complex **4** was unambiguously confirmed by X-ray diffraction analysis. Twinned crystals suitable for the structural determination (see the Experimental Section for more details) were grown in CH_2Cl_2 at room temperature within a few hours upon continuous irradiation of the solution with visible light. One molecule of **4** is shown in Figure 2, and the most significant bonding parameters are listed in the legend. Crystal data and structural refinement details are given in Table 1. Only the ipso carbons of the phenyl rings and the P−CH_2 part of the butyl chain of the SPS ligand have been displayed for clarity. As can be seen,

Chart 1

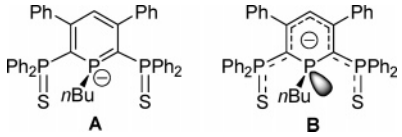

the overall geometry around the Mn center is a distorted octahedron and the ligand binds as a pincer, occupying three coordination sites in a plane. The bond lengths and angles in **4** are very similar to those of **3** with regards to the SPS ligand and the Mn−P and Mn−S distances. The exceptions are the P−S bond distances, being apparently shorter in the *fac* isomer [**3**; 2.0212(7) and 2.0145(7) Å] than in the *mer* photoproduct [**4**; 2.034(2) and 2.030(2) Å]. The most notable difference is with regards to the M−C−O bond lengths. In complex **4**, the two equatorial Mn−C46 and Mn−C48 bond distances are longer [1.858(4) and 1.831(4) Å] than those in **3** [1.792(2) and 1.783(2) Å], thereby reflecting the mutual strong trans influence of the carbonyl ligands. Consistently, the corresponding C46−O1 and C48−O3 bond lengths are found to be slightly shorter in **4** compared to **3**. This indirectly allows for a stronger binding of the axial CO ligand in **4**: the Mn−C47 distance is shorter and the C47−O2 distance longer in the *mer* isomer. These compensating changes in the Mn-to-CO π-back-donation are probably responsible for the similar CO-stretching frequencies of *fac*- and *mer*-[Mn(SPS)$(CO)_3$]. In this regard, it is noteworthy that the contributions of the carbonyl ligands to the characters of the high-lying occupied orbitals of *mer* isomer **4** and its *fac* precursor **3** (see DFT data hereafter) are comparable. Generally, larger differences are observed for the related complexes *fac*- and *mer*-[Mn(X)$(CO)_3$(α-diimine)] (X = halide). In the extreme case, *fac*-[Mn(Cl)$(CO)_3$(^{i}Pr-DAB)] (^{i}Pr-DAB = *N*,*N*′-diisopropyl-1,4-diazabuta-1,3-diene) absorbs at 2024, 1938, and 1917 cm^{-1} (in THF), while the CO-stretching bands of the corresponding *mer* isomer are found at 2051, 1972, and 1918 cm^{-1}.[46] Consistently, DFT calculations of the model complexes with H-DAB reveal much larger localization of the occupied frontier orbitals (highest occupied molecular orbital, HOMO to HOMO-5) at the carbonyl ligands of the *fac* isomer.[47] Unfortunately, short lifetimes of *mer*-[Mn(X)$(CO)_3$(α-diimine)] at room temperature (typically a few seconds)[46] preclude crystallization and comparison of X-ray structural data in this case.

The coordinated SPS ligand can be regarded either as an anionic λ^4-phosphinine (Chart 1, form A) or as a classical tertiary phosphine with the unsaturated part strongly delocalized (Chart 1, form B).[6c] The crystal structures of isomers **3** and **4** provide an important basis to rationalize the bonding situation in these complexes. In particular, the external P−C bonds in complex **3** [1.757(2) and 1.760(2) Å] and complex **4** [1.766(4) and 1.765(4) Å] are apparently shorter compared to those of λ^3-phosphinine **1** [1.826(2) and 1.835(2) Å] and to those of anion **2** [1.789(2) and 1.792(2) Å], which is

(46) Kleverlaan, C. J.; Hartl, F.; Stufkens, D. J. *J. Organomet. Chem.* **1998**, *561*, 57−65.
(47) Rosa, A.; Ricciardi, G.; Baerends, E. J.; Stufkens, D. J. *Inorg. Chem.* **1998**, *37*, 6244−6254.

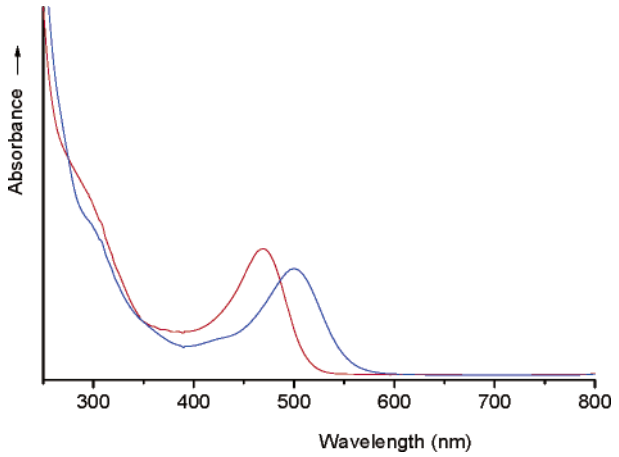

Figure 3. Electronic absorption spectra of complex **3** (red line) and its *mer* isomer **4** (blue line). Equimolar solutions in THF at 293 K.

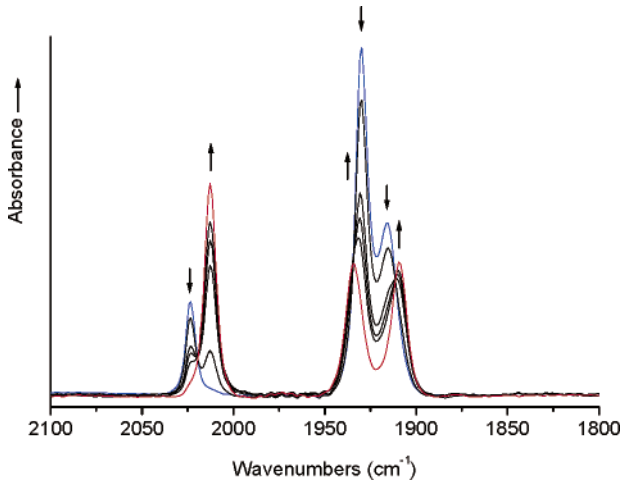

Figure 4. Thermal *mer*-to-*fac* isomerization of complex **4** (blue line) to **3** (red line) in THF monitored by IR spectroscopy on the time scale of hours.

considered as a phosphinyl-substituted pentadienyl anion (Scheme 1).[6c] Conversely, the P−S bonds are longer: 2.0212(7) and 2.0145(7) Å in complex **3**, 2.034(2) and 2.030-(2) Å in complex **4**, but merely 1.956(1) and 1.953(1) Å in **1** and 1.974(2) and 1.968(2) Å in anion **2**. For comparison, a fairly short P═S bond also exists in triphenylphosphine sulfide [1.950(3) Å][48] and its orthomanganated form in the complex η^2-*C*,*S*-[2-(diphenylthiophosphinyl)phenyl]-dicarbonylbis(trimethyl phosphite)manganese [1.996(1) Å].[49] The internal P−C bonds in complexes **3** and **4** have comparable lengths [1.785(2) and 1.800(2) Å in **3** and 1.784-(4) and 1.783(4) Å in **4**]. These data suggest that the contribution of the delocalized phosphine form B (Chart 1) of the coordinated SPS ligand in **3** and, in particular, its *mer* isomer **4** is important, if not predominant. A very similar situation has been encountered in the square-planar complex [Pd(SPS)Cl].[6a]

(Photo)isomerization and Luminescence Properties. The *fac* isomer of [Mn(SPS)(CO)$_3$] (**3**) shows in the visible region an intense absorption band at 471 nm, with molar absorption coefficient $\epsilon_{max} = 9150\ M^{-1}\ cm^{-1}$ (THF, 293 K; Figure 3). At shorter wavelengths, there is a poorly resolved lower-intensity absorption up to 330 nm and a shoulder at ca. 300 nm preceding an intense absorption below 250 nm. The band at 471 nm is not solvatochromic, and its absorption maximum does not shift even for complex **3** dispersed in a KBr pellet. A similar band appears in the UV−vis spectrum of the corresponding, although photostable, rhenium complex.[50] These observations point to an electronic transition with a negligible charge-transfer character and a small dipole-moment change in the excited state. Consistently with this presumption, an intraligand (IL), largely SPS-localized nature of this transition has been unambiguously proven by DFT calculations presented hereafter.

Irradiation into the visible absorption band of complex **3** causes a very efficient photoreaction, with a quantum yield as high as 0.80 ± 0.05 at $\lambda_{exc} = 460$ nm (see the Experimental Section), converting it into *mer* isomer **4**. The geometry has been unambiguously confirmed by the determined crystal structure of the photoproduct. It complies with the spectral changes in the IR CO-stretching region accompanying the photoreaction, with intensity patterns characteristic for a *fac*-to-*mer* conversion of a tricarbonyl complex (Figure 4 and the preceding paragraph). The efficient photoisomerization is also induced by UV-light excitation using Hg or Xe lamps (or simply with sunlight), suggesting its origin solely from a low-lying excited state. Detailed characterization of the optically populated and photoreactive excited states and a study of the mechanism of the photoisomerization are beyond the scope of this publication. Further research is underway to examine the intimate reaction mechanism by time-resolved spectroscopic techniques. Nevertheless, some conclusions can be drawn from comparison with related complexes and from analysis of emission spectra (see below). First of all, the photostability of *fac*-[Re(SPS)-(CO)$_3$] displaying a nearly identical visible absorption spectrum[50] suggests that the photoisomerization of complex **3** does not occur directly from the optically populated lowest ^{1}IL state (see below) but that another excited state is involved. A similar difference in the photochemical behavior was observed between (a) the highly photoreactive complex *fac*-[Mn(Br)(CO)$_3$(tmbp)][51] and photostable *fac*-[Re(Cl)(CO)$_3$-(tmbp)] (tmbp = 4,4′,5,5′-tetramethyl-2,2′-biphosphinine)[52] and (b) the photoreactive complexes *fac*-[Mn(X)(CO)$_3$(α-diimine)] (X = halide)[10] and their photostable Re deriva-

(48) Codding, P. W.; Kerr, K. A. *Acta Crystallogr.* **1978**, *34B*, 3785−3787.

(49) Depree, G. J.; Childerhouse, N. D.; Nicholson, B. R. *J. Organomet. Chem.* **1997**, *533*, 143−151.

(50) Doux, M.; Mézailles, N.; Ricard, L.; Le Floch, P.; Vaz, P. D.; Calhorda, M.-J.; Mahabiersing, T.; Hartl, F., unpublished results.

(51) Hartl, F.; Mahabiersing, T.; Le Floch, P.; Mathey, F.; Ricard, L.; Rosa, P.; Záliš, S. *Inorg. Chem.* **2003**, *42*, 4442−4455.

(52) (a) Mathey, F.; Le Floch, P. *Chem. Ber.* **1996**, *129*, 263−268. (b) Hartl, F., unpublished results. The complex *fac*-[Re(Cl)(CO)$_3$(tmbp)] was obtained by the reaction of [Re(Cl)(CO)$_3$(MeCN)$_2$] and tmbp (1.1 equiv, in 50 mL of Et$_2$O/3 mL of THF under reflux). After evaporation of the solvents and washing with cold Et$_2$O, the product was isolated as a yellow crystalline solid in 85% yield. ^{1}H NMR (CDCl$_3$): δ 2.47 (bs, 12 H), 8.20−8.31 (m, 4H). ^{31}P NMR (CDCl$_3$): δ 176.47. IR (CH$_2$-Cl$_2$): 2046s, 1978m, and 1929m cm^{-1}. The complex is photostable and shows in CH$_2$Cl$_2$ at room temperature a steady-state emission at $\lambda_{max} = 639$ nm upon excitation into the nonsolvatochromic visible band at 400 nm consisting of three maxima separated by approximately 1000 cm^{-1}.

tives.[53] The *fac*-to-*mer* photoisomerization of *fac*-[Mn(X)(CO)$_3$(α-diimine)] is triggered by population of a mixed metal- and halide-to-diimine charge-transfer (MLCT/XLCT) excited state corresponding to the main absorption band in the visible spectral region.[10,46,47] Interaction (avoided crossing) of the optically prepared charge-transfer state with higher-lying repulsive excited states (for example, of LF origin) leads to a dissociative potential energy surface. This process causes fast CO dissociation and movement of the halide ligand, resulting in the formation of the *mer* isomer. An alternative reaction mechanism may involve a lower-lying dissociative LF excited state populated by state crossing along the reaction coordinate.[54,55] The photoisomerization of complex **3** is also believed to proceed via an ultrafast CO-loss reaction. The recently observed CO photosubstitution of **3** with triethyl phosphite producing a dicarbonyl complex and the results of preliminary picosecond time-resolved IR spectroscopic measurements are in favor of this pathway.[56]

Photoisomer **4** absorbs strongly at 498 nm in THF, with $\epsilon_{max} = 8500\ M^{-1}\ cm^{-1}$ (Figure 3). The shift of the intense IL absorption to a lower energy compared to precursor **3** can be understood on grounds of DFT and electrochemical data (see below). Complex **4** converts smoothly back to *fac* isomer **3** in the dark within ca. 8 h at 293 K, as revealed by UV−vis and IR (Figure 4) monitoring. The slow thermal rearrangement and the inherent photostability of complex **4** allowed its crystallization from a THF solution upon continuous irradiation with a medium-pressure Hg lamp. The long lifetime of *mer* isomer **4** is remarkable, being in sharp contrast to much shorter-lived complexes *mer*-[Mn(X)(CO)$_3$(α-diimine)] (X = halide). The latter compounds isomerize back to the *fac* isomers with lifetimes strongly dependent on the nature of the halide and α-diimine ligands, with the primary reaction step involving temporary cleavage of the Mn−X or Mn−N bonds.[46] The strongly bound and bulky SPS ligand in complex **4** may form an obstacle for a dissociative mechanism, which increases the lifetime. It is noteworthy that probably a nondissociative twist mechanism operates in the case of *fac*-to-*mer* isomerization of *fac*-[Mn(Br)(CO)$_3$(P−P)]$^+$ (P−P = bidentate phosphine) while the neutral complexes *mer*-[Mn(Br)(CO)$_3$(P−P)] do not isomerize at all, despite the *fac* isomer being thermodynamically favored.[57]

Both isomers **3** and **4** are luminescent in the visible region (Figure 5). The emission of photoreactive *fac* isomer **3** at 566 nm is weak, with the emission quantum yield increasing from 1.1×10^{-4} (in aerated THF) and 4.0×10^{-4} (deaerated THF) for $\lambda_{exc} = 340$ nm to 2.8×10^{-4} (aerated THF) and 5.1×10^{-4} (deaerated THF) for $\lambda_{exc} = 446$ nm (i.e., exciting directly to the low-energy ^{1}IL electronic transition; see below). The sensitivity to $^3O_2$ quenching indicates that the emission occurs from a triplet excited state living at least a few nanoseconds. Upon photoisomerization to **4**, the emission intensity increases about 5 times and the emission maximum shifts to 585 nm (Figure 5), in agreement with the small energy difference between the corresponding ^{1}IL absorptions (Figure 3). Notably, the small Stokes shifts of the emission maxima testify to little distortion of the complex geometries in the IL excited states. The higher emission intensity of **4** is ascribed to the photostability of the *mer* isomer. In the case of *fac* isomer **3**, the population of the emitting, most likely ^{3}IL, state from the optically prepared excited state (the relaxation pathway) is partially quenched by presumably adiabatic evolution to a dissociative continuum and ultrafast CO dissociation (the reaction pathway),[56] as discussed above. In the case of photostable **4**, the low-lying ^{3}IL excited state most likely behaves as a trapping state, which results in the increased emission intensity. Time-resolved experiments are to be carried out to provide more information on the nature of the emitting excited states.

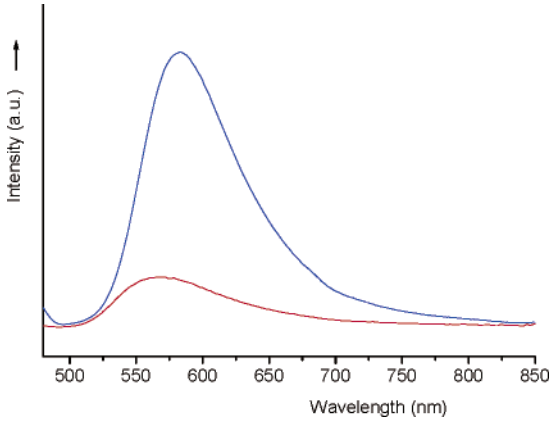

Figure 5. Emission spectra of complexes **3** (red line) and **4** (blue line). Equimolar solutions in THF at 293 K.

DFT Calculations. DFT calculations were conducted to confirm the thermodynamic stability of complex **3** and to interpret the photochemical behavior and photophysical properties of **3** and **4** (see above), as well as their redox properties that are described hereafter. Owing to the large size of the complexes, the calculations were performed on model complexes **3m** and **4m**, in which all phenyl groups were substituted by H atoms and the *n*-Bu chain was replaced by a methyl group. These calculations were conducted with the G03/B3PW91 and *ADF2004* sets of programs (see Computational Details in the Experimental Section). Some of the geometrical data are summarized in Table 2. As can be seen, there is a good agreement between the theoretical and experimental structures (almost all of the experimental values are reproduced within 0.01 Å). The exception concerns the Mn−S bonds that are overevaluated: by 0.078 Å for **3m** and 0.045 Å for **4m** with G03 and slightly less with ADF. From an energy point of view, complex **3m** is thermodynamically more stable than its *mer* isomer **4m** (by −9.4 kcal mol^{-1} with G03 and −11.3 kcal mol^{-1} with ADF), thus confirming the experimental result.

(53) Rossenaar, B. D.; Stufkens, D. J.; Vlček, A., Jr. *Inorg. Chem.* **1996**, *35*, 2902−2909.
(54) Farrell, I. R.; Vlček, A., Jr. *Coord. Chem. Rev.* **2000**, *208*, 87−101.
(55) Vlček, A., Jr.; Farrell, I. R.; Liard, D. J.; Matousek, P.; Towrie, M.; Parker, A. W.; Grills, D. C.; George, M. W. *Dalton Trans.* **2002**, 701−712.
(56) Hartl, F., upublished results. Preliminary time-resolved IR experiments show that the photochemical conversion of complex **3** into its *mer* isomer **4** proceeds via a dicarbonyl transient absorbing at 1943 and 1853 cm^{-1} (in THF), which is formed within ca. 200 ps and rearranges to **4** within ca. 1 μs.
(57) Bond, A. M.; Grabaric, B. S.; Jackowski, J. J. *Inorg. Chem.* **1978**, *17*, 1013−1018.

Table 2. Selected Distances (Å) and Angles (deg) for Complexes **3** and **4** and DFT-Calculated (G03/B3PW91 and ADF2004) Structures for Models **3m** and **4m**

complex	**3**	**3m**		**4**	**4m**	
method	X-ray	G03	ADF	X-ray	G03	ADF
P1−C2	1.785(2)	1.795	1.802	1.783(4)	1.795	1.804
C2−C3	1.413(3)	1.395	1.395	1.398(5)	1.392	1.393
C3−C4	1.400(3)	1.404	1.405	1.413(5)	1.405	1.404
P2−C2	1.760(2)	1.753	1.756	1.765(4)	1.760	1.761
P2−S1	2.0212(7)	2.019	2.018	2.034(2)	2.026	2.028
P1−C(R)	1.838(2)	1.835	1.836	1.832(4)	1.837	1.841
Mn−P1	2.2937(6)	2.324	2.294	2.2937(6)	2.298	2.300
Mn−S1	2.4002(6)	2.480	2.473	2.401(1)	2.449	2.419
Mn−CO	1.792(2)	1.776	1.787	1.831(4)	1.837	1.855
	1.829(2)	1.814	1.829	1.797(4)	1.801	1.782
	1.783(2)	1.776	1.787	1.858(4)	1.827	1.855
C−O	1.155(3)	1.159	1.144	1.151(5)	1.152	1.178
	1.144(3)	1.152	1.159	1.158(5)	1.156	1.135
	1.159(3)	1.159	1.155	1.147(4)	1.155	1.134
P1−C2−C3	116.8(1)	119.5	119.5	119.5(3)	120.0	120.9
C2−C3−C4	122.4(2)	124.5	124.4	122.6(3)	124.4	124.5
C3−C4−C5	124.0(2)	121.2	121.6	125.0(3)	122.0	122.1
C6−P1−C2	100.72(8)	99.6	99.5	100.8(2)	100.2	99.6
Σ angles P1	307.4	310.2	310.1	311.4	310.5	310.2

To assign the low-lying electronic transitions in the experimental spectra, TD-DFT calculations of the model complexes were carried out using both ADF and G03/B3LYP (see the Experimental Section for details). Notably, ADF led, in the case of **4m**, to a weak absorption band at ca. 700 nm, which was not encountered in the experimental spectrum of complex **4**. The discrepancy of the ADF result probably arises from a different arrangement of the frontier orbitals, namely, the HOMO and HOMO-1 in **3m**, which interchange their positions in **4m**. This switch does not influence the geometries because both orbitals are occupied. Therefore, we decided to use in all of the following discussion only the results from G03 because the different methodological approach (hybrid functionals) offers a better description.

The energies and composition of the frontier molecular orbitals of **3m** and **4m** are given in Table 3. Their representations are depicted in Figures 6 and 7. Importantly, both for the *fac* and *mer* isomers, **3m** and **4m**, respectively, the HOMO and lowest unoccupied molecular orbital (LUMO) are ligand-centered orbitals, localized on the PC_5H_3 ring of the pincer ligand, deriving largely from two π^* orbitals of the pentadienyl anion. The LUMO also features a small participation of the two P atoms of the ligand arms.

In **3m**, the H-1, H-3, and H-4 are the Mn-based "t_{2g}" orbitals, while the H-2 can be described essentially as the out-of-phase combination of two S lone pairs, with some Mn participation. The L+1 is the $x^2 - y^2$ "e_g" orbital, σ-antibonding between Mn and S atoms and the equatorial carbonyls and π-antibonding toward the axial carbonyl. The L+2 differs by being π-bonding toward the axial carbonyl but σ-antibonding with respect to the equatorial CO ligands. The L+3 is π-antibonding between Mn and the equatorial carbonyls, with a larger contribution from the side-arm P atoms.

The frontier orbitals of *mer* isomer **4m** do not differ significantly. The three "t_{2g}" orbitals are H-1, H-2, and H-3, while the H-4 is mainly localized at S. The L+1 is also the $x^2 - y^2$ "e_g" orbital, σ-antibonding between Mn and S. The

Table 3. Composition (%) and Energies (eV) of Frontier Molecular Orbitals of the Model Compounds of *fac*- and *mer*-[Mn(SPS)(CO)$_3$] (**3m** and **4m**, respectively) from G03/B3LYP (**L** = LUMO; **H** = HOMO)

orbital		*E* (eV)	Mn	ΣSPS[a]	ΣCO
		Compund **3m**			
86a	H-4	−7.03	55.7	29.7 (20.1)	14.5
87a	H-3	−6.88	78.5	6.4	15.1
88a	H-2	−6.44	16.4	79.0 (63.6)	4.6
89a	H-1	−6.21	52.7	39.9 (30.0)	7.8
90a	**H**	**−5.73**	**2.0**	**89.2**	**8.8**
91a	**L**	**−1.88**	**1.0**	**97.9**	**0.8**
92a	L+1	−1.29	37.0	45.2 (31.8)	17.7
93a	L+2	−1.26	20.6	69.0 (27.2)	10.4
94a	L+3	−0.64	15.0	78.3 (23.9)	6.7
95a	L+4	−0.48	20.5	54.4	25.1
		Compund **4m**			
86a	H-4	−6.98	12.4	78.4 (56.6)	9.2
87a	H-3	−6.74	61.6	17.8	20.6
88a	H-2	−6.23	73.1	16.4	10.5
89a	H-1	−5.74	57.5	36.5 (27.9)	5.9
90a	**H**	**−5.62**	**6.1**	**81.8**	**12.1**
91a	**L**	**−2.13**	**3.6**	**94.4**	**2.1**
92a	L+1	−1.31	30.4	66.6 (25.1)	3.0
93a	L+2	−1.21	19.8	51.1 (30.8)	29.0
94a	L+3	−0.84	13.8	63.2 (22.2)	23.0
95a	L+4	−0.56	12.0	78.8 (31.5)	9.2

[a] S contribution above 20% in the parentheses.

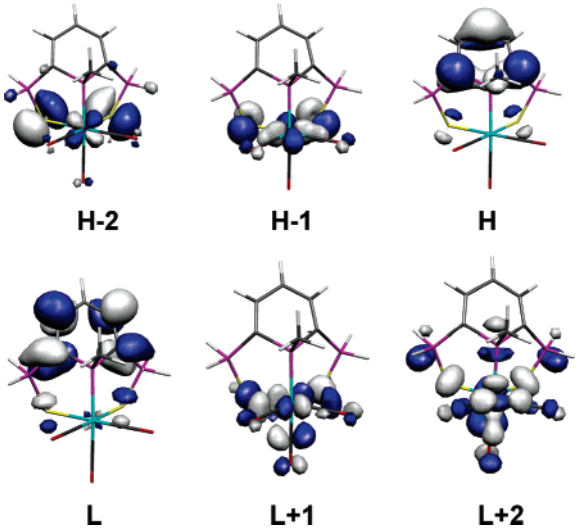

Figure 6. Frontier orbitals of model complex **3m** from G03/B3LYP in a MOLEKEL representation.

L+2 and L+3 have a strong contribution from the π^* orbitals of the equatorial carbonyls.

The most intense calculated absorption band in the visible spectral region (Table 4) can be assigned for both complexes as a HOMO-to-LUMO electronic transition having an IL character. Although the calculated electronic transitions are shifted to higher energies compared to the experimental UV−vis spectra (Figure 3), the trends are the same in the calculated and experimental values, with the absorption bands of the *fac* isomer at higher energies (Figure 8). The other calculated transitions at higher energies exhibit much smaller oscillator strengths and are indeed poorly resolved in the experimental spectra.

The calculated smaller HOMO−LUMO energy gap for *mer* isomer **4** and the spectral red shift of its intense lowest-energy IL (HOMO-to-LUMO) absorption band compared to

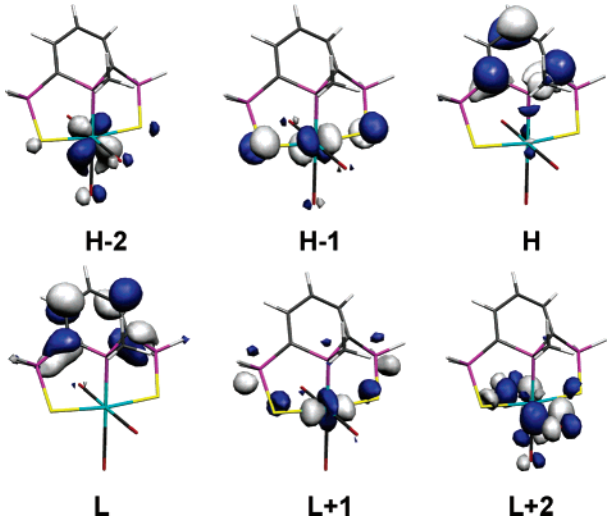

Figure 7. Frontier orbitals of model complex **4m** from G03/B3LYP in a MOLEKEL representation.

Table 4. Low-Energy Excitation Energies, Wavelengths, and Oscillator Strengths (OS) for the Model Compounds *fac*- and *mer*-[Mn(SPS)(CO)$_3$] (**3m** and **4m**, respectively) from G03/B3LYP

excitation	composition (%)	E (eV)	λ_{max} (nm)	λ_{max}[a] (nm)	OS ($\times 10^3$)
	Compound **3m**				
1	78 (H → L)	3.23	384	471	95.7
2	27 (H-4 → L+1), 24 (H-2 → L+2), 23 (H-1 → L+1)	3.50	354		3.6
3	83 (H → L+1)	3.54	350		8.2
4	92 (H-2 → L)	3.89	319	*b*	13.3
5	49 (H-2 → L+1), 19 (H-4 → L+1), 9 (H → L+4)	4.34	286	*b*	20.6
	Compound **4m**				
1	84 (H → L)	2.84	436	498	93.5
2	96 (H-1 → L+1)	3.05	407		4.6
3	94 (H → L+2)	3.54	350	430 (sh)	13.3
4	81 (H → L+3)	3.91	317		4.1
5	78 (H-2 → L+2)	3.96	313		9.1
6	59 (H-4 → L)	4.13	300		5.1

[a] Experimental UV−vis absorption spectra in THF at 293 K (see Figure 3). [b] Poorly resolved.

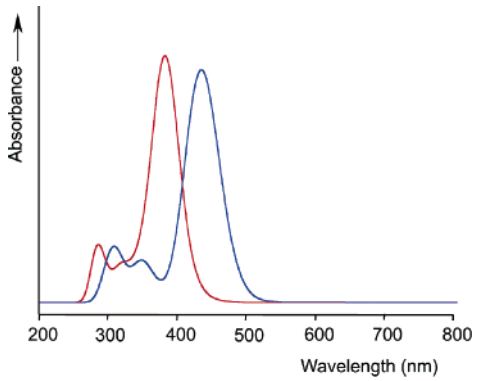

Figure 8. SWizard simulation of the G03-calculated electronic absorption spectra of model complexes **3m** (red line) and **4m** (blue line) from G03/B3LYP. The corresponding experimental spectra of complexes **3** and **4** are depicted in Figure 3.

fac isomer **3** are fully consistent with data obtained from spectroelectrochemical investigations of the redox properties of both isomers (see below).

Cyclic Voltammetry. The cyclic voltammogram of *fac* isomer **3**, recorded in THF at 293 K at $v = 100$ mV s^{-1}, shows a fully reversible anodic wave at $E_{1/2} = +0.34$ V vs Fc/Fc$^+$ (Figure 9). The stability of the one-electron-oxidized radical cation, **3**$^{\bullet+}$, at room temperature is unusual for a tricarbonylmanganese complex and indirectly points to the involvement of the SPS-localized HOMO (Table 3) in this process. In the cathodic region, fully reversible reduction of *fac* isomer **3** to **3**$^{\bullet-}$ occurs at $E_{1/2} = -2.34$ V. This step is followed by irreversible reduction of **3**$^{\bullet-}$ to **3**$^{2-}$ at $E_{p,c} = -2.82$ V. A reverse voltammetric scan triggered beyond the second cathodic wave leads to the appearance of an irreversible anodic peak at $E_{p,a} = -1.05$ V belonging to oxidation of a secondary reduction product formed by a chemical reaction of **3**$^{2-}$. A detailed investigation of this electrochemical process was beyond the scope of this study.

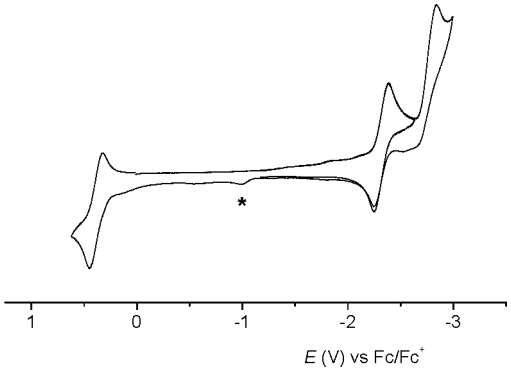

Figure 9. Cyclic voltammogram of complex **3**. The asterisk marks the anodic wave of a secondary reduction product formed by two-electron reduction of **3** at the second cathodic wave. Conditions: THF/Bu$_4$NPF$_6$, 293 K, Pt disk microelectrode, $v = 100$ mV s^{-1}.

The photochemical conversion of **3** to its *mer* isomer **4**, performed in situ in the cyclic voltammetric cell and monitored by IR spectroscopy, was reflected in a negative shift of the reversible anodic wave to $E_{1/2} = -0.08$ V. The ordinary cyclic voltammogram of *mer* isomer **4** in the cathodic region showed two waves at the same electrode potentials as those recorded for its precursor **3** ($v = 100$ mV s^{-1}). The corresponding thin-layer cyclic voltammogram obtained with a spectroelectrochemical cell ($v = 2$ mV s^{-1}) and parallel monitoring of the cathodic scan with IR spectroscopy revealed rapid conversion of **4** to neutral **3** (Figure 10). No apparent cathodic wave due to **4** or CO-stretching bands of primarily reduced radical anion **4**$^{\bullet-}$ could be detected during this process. The electroinduced reversal of the photochemical *fac*-to-*mer* isomerization is thus incomparably faster than the corresponding slow thermal *mer*-to-*fac* isomerization (see above). The successive cathodic wave of product **3** was well observable in the course of the thin-layer voltammetric scan. The corresponding one-electron reduction of the *fac* isomer gave smoothly its stable radical anion **3**$^{\bullet-}$ (see below). From this behavior, it can be deduced that *mer* isomer **4** reduces at a less negative electrode potential than *fac* isomer **3**.

The less positive oxidation potential (by −0.42 V) and a less negative reduction potential of *mer* isomer **4** compared to thermodynamically more stable *fac* isomer **3** nicely correlate with the smaller HOMO−LUMO gap in the case of **4**, as calculated by the DFT method: $\Delta(\Delta E_{HOMO-LUMO})$

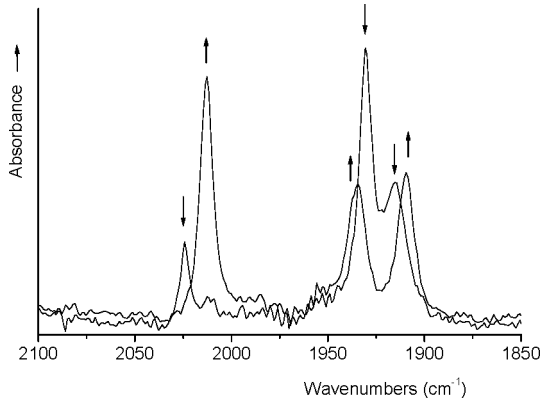

Figure 10. IR spectral changes in the CO-stretching region due to the conversion of complex **4** into its *fac* isomer **3** induced by electrochemical reduction within an OTTLE cell. Conditions: THF, 293 K.

= 0.36 eV (Table 3). This difference, which mainly arises from the stabilization of the HOMO of *fac* isomer **3**, is also reflected in the lower energy of the largely HOMO-to-LUMO IL electronic transition of complex **4** compared to **3** (Table 4 and Figures 3 and 8): 0.16 eV (measured) vs 0.36 eV (calculated).

Spectroelectrochemistry. Spectroelectrochemical experiments, supported by the DFT calculations, were conducted with the aim to collect spectroscopic data for a convincing assignment of the frontier orbitals of the [Mn(SPS)(CO)$_3$] isomers **3** and **4** and a description of their radical redox products.

However, attempts to characterize *mer* isomer **4** in this way were unsuccessful. IR spectroelectrochemical measurements in THF at room temperature showed efficient electrode-catalyzed conversion of **4** to *fac* isomer **3** induced by the one-electron reduction to radical anion **4**$^{\bullet-}$ (see above). Electrochemical one-electron oxidation to radical cation **4**$^{\bullet+}$ mainly resulted in a rapid decarbonylation process, most likely caused by weak Mn−CO bonds of the trans-oriented equatorial carbonyls in the oxidized complex. Importantly, isomer **3** was also formed as a minor side product of the oxidation. The same result was obtained when **4** was oxidized chemically with 1 mol equiv of [$FeCp_2$][BF_4]. Apparently, the thermodynamic instability of *mer*-[Mn(CO)$_3$(SPS)] becomes more pronounced upon the one-electron reduction and oxidation of the complex.

One-electron oxidation of *fac* isomer **3** in THF at room temperature in a thin-layer cell, monitored in situ by IR spectroscopy, resulted in a high-frequency shift of the ν(CO) stretching bands of the parent complex (2013vs, 1933s, and 1909s cm^{-1}) to a *fac*-geometry band pattern of **3**$^{\bullet+}$ at 2033s, 1961m, and 1935m cm^{-1} (Figure 11). A similar situation applied for the dichloromethane solution where the wavenumbers are 2014, 1936, and 1907 cm^{-1} for **3** and 2037, 1967, and 1934 cm^{-1} for its radical cation. The magnitude of the spectral shift in the carbonyl region (20−30 cm^{-1}) reveals a ligand-localized process, in full agreement with the SPS character of the HOMO of complex **3** (Table 3 and Figure 6). In both electrolytes, however, radical cation **3**$^{\bullet+}$ is accompanied by an unassigned side product absorbing at 2075 and 2021 cm^{-1} (in dichloromethane; wavenumbers

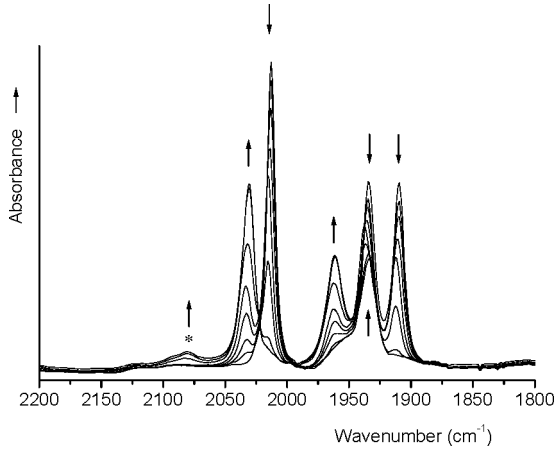

Figure 11. IR spectral changes in the CO-stretching region accompanying the one-electron oxidation of *fac* isomer **3** within an OTTLE cell. Conditions: THF, 293 K. The asterisk denotes a side product.

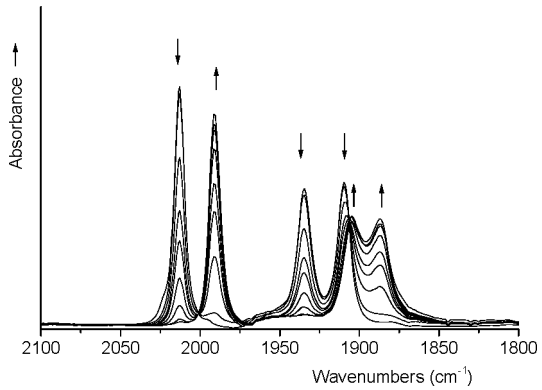

Figure 12. IR spectral changes in the CO-stretching region accompanying the one-electron reduction of *fac* isomer **3** within an OTTLE cell. Conditions: THF, 293 K.

obtained from difference absorption spectra), which is formed mainly at the end of the anodic process. The secondary reactivity of **3**$^{\bullet+}$ is much less pronounced in THF than in dichloromethane. Lowering the temperature of the solution in dichloromethane to 223 K had a negligible effect on the IR spectroelectrochemical result.

The electrochemical oxidation of complex **3** to **3**$^{\bullet+}$ in THF was merely accompanied by broadening of the IL absorption band at 470 nm (cf. Figure 3) and a decrease of its intensity. The shoulder at 300 nm shifted to 320 nm, and its intensity also decreased. Departure from isosbestic points observed at 510, 385, 330, and 280 nm in the final stage of the electrolysis documented the instability of **3**$^{\bullet+}$ at higher concentrations.

The electrochemical one-electron reduction of complex **3** in THF at room temperature produced stable radical anion **3**$^{\bullet-}$. In the IR spectra, the ν(CO) bands of the parent complex (2013, 1933, and 1909 cm^{-1}) were smoothly replaced by a new set at 1990, 1904, and 1887 cm^{-1} (Figure 12). Also in this case, the magnitude of the shift corresponds to a SPS-localized reduction, as predicted by the DFT calculations of LUMO character (Table 3 and Figure 6). In the course of the cathodic electrolysis, the yellow color of the solution turned red. The isosbestic UV−vis spectral changes accompanying the formation of **3**$^{\bullet-}$ are depicted in Figure 13.

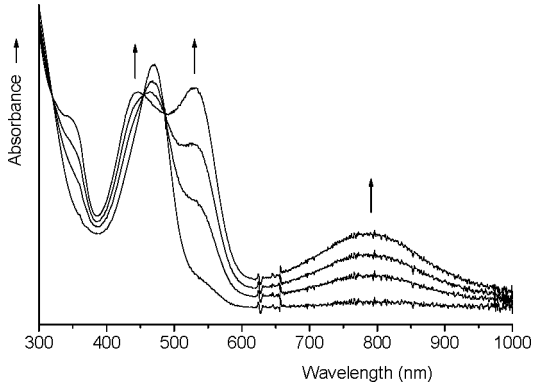

Figure 13. UV−vis spectral changes accompanying the one-electron reduction of *fac* isomer **3** within an OTTLE cell. Conditions: THF, 293 K.

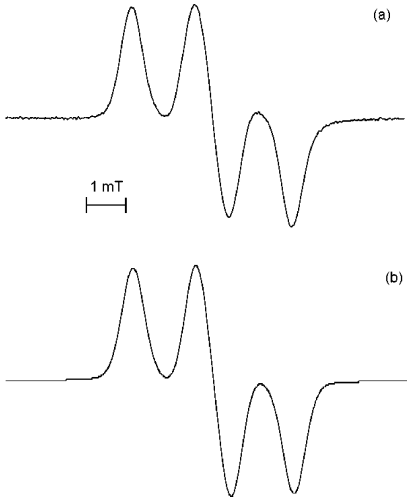

Figure 14. Experimetal (a) and simulated (b) EPR spectra of radical anion $\mathbf{3}^{\bullet-}$ generated by electrochemical one-electron reduction of parent complex **3** in THF at 243 K within a spectroelectrochemical cell.

Consistent with the reduction of the SPS ligand, all new electronic transitions in the visible region are assumed to have an SPS IL character. Virtually the same electronic spectrum was also recorded for the corresponding radical anionic Re complex.[50] The exact assignment of the absorption bands was beyond the scope of this work.

The predominant localization of the unpaired electron in the largely SPS-based SOMO of radical anion $\mathbf{3}^{\bullet-}$ was confirmed by its EPR spectrum recorded in THF at 243 K at $g = 2.0066$ (Figure 14). Satisfactory simulation of the triplet signal revealed hyperfine splitting by two equivalent ^{31}P nuclei of the $-Ph_2P{=}S$ side arms, with $a_P = 1.41$ mT. In addition to the line width of 0.6 mT, the satisfactory reproduction of the spectral shape also required the involvement of unresolved sextet splitting by ^{55}Mn ($I = {}^5/_2$), with $a_{Mn} \sim 0.2$ mT. These data correspond to a singly occupied frontier orbital similar to the LUMO of **3** depicted in Figure 6, which shows the *n*-BuP phosphorus and the C−H bond of the SPS ring lying in a nodal plane, together with a limited contribution from the Mn center.

Conclusions

Several conclusions regarding the SPS ligand **2** (Scheme 1 and Chart 1) can be drawn from the present study. Most importantly, this anionic pincer ligand is sufficiently flexible to stabilize the *fac* and *mer* geometry of $[Mn(SPS)(CO)_3]$. This remarkable property points to its great potential in coordination chemistry (materials) and catalysis. The long lifetime of *mer* isomer **4** is unusual and facilitates its thorough crystallographic, spectroscopic, and electrochemical characterization and comparison with *fac* isomer **3**. The second important conclusion is that the frontier orbitals, the HOMO and LUMO, of both isomers are largely localized on the SPS ligand, with profound consequences for their spectroscopic properties and redox behavior. In particular, not only the electrochemical one-electron reduction but also oxidation of *fac* isomer **3** is reversible. This is uncommon for manganese(I) carbonyl complexes with other types of noninnocent ligands such as α-diimines,[10c] with the exception of redox series based on dioxolene ligands.[58] Work is in progress[50] to describe the redox behavior of **3** in more detail, in particular the reactivity of dianion $\mathbf{3}^{2-}$ produced in the second cathodic step. The quenched luminescence of complex **3** is explained by its photoreactivity, most likely from a low-lying CO-dissociative excited state. The excited states and photophysical properties of *fac* isomer **3** and its Re derivative,[50] as well as *mer* isomer **4** have been under detailed investigation, using time-resolved spectroscopic techniques.[56]

Acknowledgment. We are grateful for the financial support provided by the CNRS, the Ecole Polytechnique, the DGA, and the Council for Chemical Sciences of The Netherlands Organization for Scientific Research (Grant NWO R71-140). This work is also part of the European collaborations COST Action D14, Project D14/0001/99, and Action D29, Project D29/0012/24. Ron T. F. Jukes (Amsterdam) is acknowledged for his help with the determination of the luminescence quantum yields and Márcia S. Mora (Lisbon) for her assistance with the spectroelectrochemical experiments. P.D.V. thanks FCT for a postdoctoral grant.

Supporting Information Available: X-ray structure determination for complexes **3** and **4**, including tables of crystal data, atomic coordinates and equivalent isotropic displacement parameters, bond distances and angles for all non-hydrogen atoms, anisotropic displacement parameters, and hydrogen coordinates. Crystallographic data in CIF format. This material is available free of charge via the Internet at http://pubs.acs.org.

IC050774M

(58) (a) Hartl, F.; Stufkens, D. J.; Vlček, A., Jr. *Inorg. Chem.* **1992**, *31*, 1687−1695. (b) Hartl, F. *Inorg. Chim. Acta* **1995**, *232*, 99−108.